Neurobiology of Disease 197 (2024) 106536

Contents lists available at ScienceDirect

Neurobiology of Disease

journal homepage: www.elsevier.com/locate/ynbdi

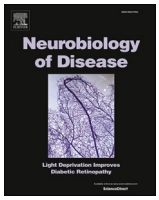

Targeting autophagy impairment improves the phenotype of a novel CLN8 zebrafish model

Maria Marchese [a,*], Sara Bernardi [a,b], Asahi Ogi [a], Rosario Licitra [a], Giada Silvi [a], Serena Mero [a], Daniele Galatolo [a], Nicola Gammaldi [a,c], Stefano Doccini [a], Gian Michele Ratto [d], Simona Rapposelli [e], Stephan C.F. Neuhauss [f], Jingjing Zang [f], Silvia Rocchiccioli [g], Elena Michelucci [g,h], Elisa Ceccherini [g], Filippo M. Santorelli [a,*]

[a] Department of Neurobiology and Molecular Medicine, IRCCS Fondazione Stella Maris, Calambrone, Pisa, Italy
[b] Department of Biology, University of Pisa, Pisa, Italy
[c] Department of Neurosciences, Psychology, Drug Research and Child Health (NEUROFARBA), University of Florence, Florence, Italy
[d] National Enterprise for NanoScience and NanoTechnology (NEST), Istituto Nanoscienze, Consiglio Nazionale delle Ricerche (CNR) and Scuola Normale Superiore, Pisa, Italy
[e] University of Pisa, Department of Pharmacy, Pisa, Italy
[f] University of Zurich, Department of Molecular Life Sciences, Zurich, Switzerland
[g] Institute of Clinical Physiology, National Research Council, Pisa, Italy
[h] Institute of Chemistry of Organometallic Compounds, National Research Council, Pisa, Italy

ARTICLE INFO

Keywords:
Neuronal ceroid lipofuscinosis 8
Zebrafish
Autophagy
Drug screening

ABSTRACT

CLN8 is an endoplasmic reticulum cargo receptor and a regulator of lysosome biogenesis whose loss of function leads to neuronal ceroid lipofuscinosis. CLN8 has been linked to autophagy and lipid metabolism, but much remains to be learned, and there are no therapies acting on the molecular signatures in this disorder. The present study aims to characterize the molecular pathways involved in CLN8 disease and, by pinpointing altered ones, to identify potential therapies. To bridge the gap between cell and mammalian models, we generated a new zebrafish model of CLN8 deficiency, which recapitulates the pathological features of the disease. We observed, for the first time, that CLN8 dysfunction impairs autophagy. Using autophagy modulators, we showed that trehalose and SG2 are able to attenuate the pathological phenotype in mutant larvae, confirming autophagy impairment as a secondary event in disease progression. Overall, our successful modeling of CLN8 defects in zebrafish highlights this novel *in vivo* model's strong potential as an instrument for exploring the role of CLN8 dysfunction in cellular pathways, with a view to identifying small molecules to treat this rare disease.

1. Introduction

The term neuronal ceroid lipofuscinosis (NCL) refers to a group of lysosomal storage disorders, with different ages at onset, in which impaired lysosomal function of many tissue and cell types, both neuronal and extra-neuronal, causes accumulation of autofluorescent storage material. However, the disease mainly affects the central nervous system and eyes. Common symptoms include progressive loss of vision, mental and motor deterioration, epileptic seizures, and, in the rare adult-onset form, frank dementia (Morsy et al., 2021). The accumulated storage material resembles ceroid and lipofuscin, which accumulate during normal aging (Marotta et al., 2017; Nita et al., 2016). Currently, no curative treatments are available and all forms of NCL are fatal. Neuronal ceroid lipofuscinosis type 8 (CLN8) is a late-childhood-onset form (onset on average after 4 years of age) reported in multiple ethnicities. It accounts for 2–3% of all NCLs (Nita et al., 2016). The CLN8

Abbreviations: NCL, neuronal ceroid lipofuscinosis; FDA, U.S. Food and Drug Administration; dpf, days post fertilization; hpf, hours post fertilization; CID, collision-induced dissociation; IDA, information-dependent acquisition; CES, collision energy spread; DIA, data-independent acquisition; DEPs, differentially expressed proteins; AO, acridine orange; ERG, electroretinogram recording; LFP, local field potential; ER, endoplasmic reticulum; WT, wild-type; TTBS, Tween-Tris-buffered saline; ROI, region of interest; RMS, root mean square; NMD, nonsense-mediated mRNA decay; CTSD, cathepsin D; SCMAS, ATP synthase subunit C.

* Corresponding authors.
E-mail addresses: maria.marchese2086@gmail.com (M. Marchese), filippo3364@gmail.com (F.M. Santorelli).

https://doi.org/10.1016/j.nbd.2024.106536
Received 16 February 2024; Received in revised form 7 May 2024; Accepted 15 May 2024
Available online 17 May 2024

protein is an endoplasmic reticulum (ER)-associated membrane protein whose loss of function leads to impaired lysosomal storage (Ranta et al., 1999). di Ronza and colleagues found that CLN8 is an ER cargo receptor that, through interaction with the COPII and COPI machineries, regulates lysosome biogenesis (di Ronza et al., 2018) by transferring lysosomal enzymes from the ER to the Golgi apparatus. Impaired function of CLN8 leads to reduced clearance of protein aggregates, suggesting an alteration of autophagy, as already reported in several mouse models of NCL (Leinonen et al., 2017). On the basis of earlier work (Passantino et al., 2013) suggesting that CLN8 acts on processes relevant to lipid synthesis and transport, membrane trafficking, and autophagy, through binding of its C-terminus with the inhibitor 2 of type 2 protein phosphatase, it has been hypothesized to be a regulator of cell signaling (Adhikari et al., 2019). Pesaola and colleagues provided evidence that CLN8 participates in vesicular distribution, maintenance of lysosomal pH, and normal development of the dendritic tree (Pesaola et al., 2021). All these findings show that CLN8 is involved in biologically relevant processes with potential links to the pathophysiology of NCL. Nonetheless, the scope and involvement of CLN8 in autophagy still need to be fully clarified (Kim et al., 2022), also to identify molecules of potential therapeutic value.

To date, two CLN8 animal models have been described and characterized. The first is the naturally occurring canine (English Setter) model (Katz et al., 2017), scarcely used in preclinical research. The other is the *mnd* mouse model, which carries a homozygous mutation in *Cln8* (Ranta et al., 1999) and recapitulates the typical signatures of NCL pathology, including storage of autofluorescent material, gliosis, brain and retinal degeneration, lysosomal abnormality, motor coordination impairment, and decreased learning and memory (Messer and Flaherty, 1986; Bronson et al., 1993; Traina et al., 2012; Bolivar et al., 2002); this model is valuable for investigating disease mechanisms and intracerebroventricularly delivered AAV9 gene therapy approaches.

The zebrafish is an *in vivo* tool, ideal for bridging the gap between mammalian and *in vitro* models of CLN8, since it has already been used successfully to model lysosomal storage diseases including NCLs (Mahmood et al., 2013), glycogen storage disorders, namely Pompe disease (Wu et al., 2017) and Lafora disease (Della Vecchia et al., 2022), and different forms of epilepsy (Grone et al., 2016). Moreover, it has become a leading model for large-scale screening of therapeutic compounds and for phenotype-based drug discovery (MacRae and Peterson, 2015).

With the aim of dissecting complex disease-related cellular pathways *in vivo*, we edited the gene to produce a novel *cln8* knockout model in zebrafish. We also combined cell- and behavior-based phenotypic screening of newly synthesized compounds with repurposing of FDA-approved autophagy-modulating molecules able to correct locomotor and biochemical impairment in CLN8. Together, our data show that the *cln8*$^{-/-}$ fish model is a very promising instrument for exploring mechanisms underlying disease status, with a view to developing new small-molecule approaches to NCLs.

2. Materials and methods

2.1. Zebrafish maintenance

Experiments were conducted on a *cln8*$^{-/-}$ and also on a transgenic [Tg (neurod1:GCaMP6F)] line (kindly donated by Claire Wyart of the Institut du Cerveau et de la Moelle Épinière, Paris, France) (Rupprecht et al., 2016) in the nacre (*mitfa*$^{-/+}$) background, which will henceforth be referred to as WT. We used the *mitfa*$^{-/-}$ background for calcium imaging analyses, whereas the *mitfa*$^{-/+}$ fish were used for the other experiments. We had previously verified the absence of any behavioral differences between the [*mitfa*$^{-/+}$; Tg (neurod1:GCaMP6F)] line and the standard AB line (Della Vecchia et al., 2022). The *cln8*$^{-/-}$ experimental fish were generated by intercrossing *cln8*$^{-/-}$ males and females. Adults were housed in tanks at a density of no more than five zebrafish per liter at a constant temperature of 28 °C with a 14-h light/10-h dark cycle. Zebrafish eggs and embryos were collected and grown at 28.5 °C in egg water obtained using "Instant Ocean" sea salts (60 μg/mL) (Aquarium Systems, Sarrebourg, France) and in E3 medium (292.2 mg NaCl, 12.6 mg KCl, 48.6 g mM $CaCl_2$ $2H_2O$, and 39.8 mg MgSO4, per 1 L of deionized water), respectively, according to established procedures (Westerfield, 2000). They were staged in either hours post fertilization (hpf) or days post fertilization (dpf). All compounds used for E3 medium solution preparation were purchased from Sigma-Aldrich (St. Louis, MO, USA). The generation of the mutant, using CRISPR/Cas9 technology, was performed with the ethical approval of the Italian Ministry of Health (approval n° 584/2019-PR), in accordance with the European Union's Directive 2010/63/EU on the protection of animals used for scientific purposes, under the supervision of the University of Pisa Animal Care and Use Committee, and in compliance with the 3R principles.

2.2. Establishing mutant lines

The selected sgRNA was chosen among the top targets identified by CHOPCHOP software (www.chochop.rc.fas.harvard.edu/index.php) set with NGG PAM sites and zero predicted off-targets (fewer than three mismatches in the *cln8*-targeting 20-mer). The sgRNA was designed against exon three of the *cln8* transcript (ENSDART00000148431.2) (Supplementary Table S1) and generated as already described. The sgRNA was transcribed using the Megascript T7 Transcription Kit (Invitrogen, Heidelberg, Germany) (Naef et al., 2021). The optimized Cas9 mRNA, for genome editing in zebrafish, was transcribed from a linearized template plasmid pCS2-nCas9n using the mMESSAGE mMACHINE™ SP6 Transcription Kit (Thermo Fisher Scientific, Waltham, MA, USA). RNA concentration was quantified using a NanoDrop spectrophotometer (Optosky, Xiamen, China) and diluted to 500 ng/μL. About 100 ng of *cln8*-sgRNA and 500 ng of Cas9 mRNA were co-injected into 1-cell-stage embryos to ensure high-efficiency delivery of the injected mRNA to the embryo. The volume of solution injected was ~1 nL. At least three independent injection experiments were performed with spawns from different founder fish to control for the batch effect. CRISPR/Cas 9 was used in the WT strain.

2.3. Genotyping

For mutation screening, sgRNA-injected F0 embryos, raised to adulthood and outcrossed with the Tg(neurod1:GCaMP6F) line, were used to obtain heterozygous F1 embryos. Adults potentially carrying mutations were identified by PCR and fragment analysis using genomic DNA from 16 randomly selected F1 embryos. The sequences of the primers used are listed in Supplementary Table S1. Heterozygous F1 fish carrying an 11-bp deletion mutation in the target site were selected and inter-crossed to generate the homozygous F2 *cln8*$^{-/-}$ line.

2.4. In situ hybridization

Whole-mount *in situ* hybridization was performed in 5 dpf WT larvae as described elsewhere (Marchese et al., 2016). Templates for riboprobes were generated by PCR amplification of zebrafish *cln8* transcript, using a T3 promoter sequence added to either the reverse primer (for the antisense probe) or the forward primer (for the sense control). The sequences of the primers used can be found in Supplementary Table S1.

2.5. Analysis of larval morphology

Live zebrafish were mounted on glass depression slides with 1% low melting point agarose. Images were obtained using a Leica M205FA stereomicroscope (Leica Microsystems, Wetzlar, Germany). Zebrafish standard body length, eye size, and yolk sac area were measured using Danioscope software (Noldus Information Technology Wageningen, The Netherlands) (Della Vecchia et al., 2022).

2.6. Quantitative (q)RT-PCR

Gene expression levels of *cln8* mRNA were examined using RNA pooled from WT and *cln8*$^{-/-}$ larvae. Total RNA was extracted from 30 larvae at 120 hpf using the Quick RNA Miniprep Kit (Zymo Research, Irvine, CA, USA) according to the manufacturer's instructions, and quantified with a NanoDrop™ ND-1000 spectrophotometer (Thermo Fisher Scientific). Extraction of cDNA and qRT-PCR were performed as described elsewhere (Marchese et al., 2016). Relative expression levels of each gene were calculated using the $2^{-\Delta\Delta CT}$ method (Livak and Schmittgen, 2001). The results obtained in at least three independent experiments were normalized to the expression of the housekeeping gene, *β-actin* (ENSDARG00000037746). The expression analysis of *cln8* mRNA in mutant larvae was calculated setting the mean of the controls at one, and the *p*-value was calculated using GraphPad Prism 6 software (GraphPad Software Inc., San Diego, CA, USA). The primers used are listed in Supplementary Table S1.

2.7. Western blotting

Larvae collected at 120 hpf ($n = 60$) in triplicates were lysed in RIPA buffer (Cell Signaling Technology Inc., Danvers, MA) and Western blotting was performed as described elsewhere (Di Nottia et al., 2020). In brief, 50 μg of proteins was loaded in Novex™ 8–16% Tris-Glycine Mini Gels, WedgeWell™ format (Thermo Fisher Scientific), in reducing conditions. Blots were performed using the Trans-Blot Turbo Transfer System (Bio-Rad Laboratories Inc., Berkeley, CA) and Trans-Blot® Turbo™ RTA Mini PVDF Transfer Kit (Bio-Rad Laboratories Inc.). Membranes were blocked with TBS/0.1% Tween20 (TTBS) containing 5% non-fat dry milk. Primary antibodies were incubated overnight at 4 °C in TTBS with 2.5% non-fat dry milk, whereas, as secondary antibodies, we used peroxidase-conjugated anti-mouse and anti-rabbit antibodies (Jackson Immuno Research Inc., West Grove, PA) for 1 h at room temperature in the same buffer used for the primary antibodies (2.5% non-fat dry milk in TTBS). Bands were revealed using the ChemiDoc™ Imaging System (Bio-Rad Laboratories Inc.). ImageJ software (https://imagej.nih.gov/ij/) was used for densitometry analysis. The following antibodies were used: anti-LC3 (NB100–2220, Novus Biologicals, Centennial, CO, USA; 1:1000), anti-ATG5 (NB110–53818, Novus Biologicals; 1:500), anti-Rab7 (R4779, Sigma-Aldrich; 1:2000), anti-cathepsin D (610,801, BD Biosciences, Franklin Lakes, NJ; 1:250), anti-β-actin (GTX629630, GeneTex, Irvine, CA; 1:2500), and anti-GAPDH (GTX100118, GeneTex; 1:5000).

2.8. Proteomic analysis

2.8.1. Sample preparation for mass spectrometry-based proteomics

Six pellets of whole zebrafish larvae at 5 dpf (three WT and three *cln8*$^{-/-}$, each derived from 100 larvae) were thawed, allowed to return to room temperature, treated with 200 μL of 5% (*w/v*) sodium deoxycholate (D6750, Sigma-Aldrich) aqueous solution, and incubated in a Thermomixer Compact (Eppendorf, Hamburg, Germany) for 10 min at 80 °C at 500 rpm. The samples were sonicated for 5 min (five 20-s cycles separated by 40-s intervals on ice) and clarified by centrifugation (13,000 rpm for 10 min at 4 °C). The Pierce bicinchoninic acid assay (reagent A 23228 and reagent B 1859078, Thermo Scientific, Rockford, IL) was used to determine the protein concentration of the supernatants, with serum albumin (A7906, Sigma-Aldrich) used as a standard. For each sample, 100 μg of protein was reduced with 10 mM dithiothreitol (D1 309.0010, Duchefa Biochemie, Haarlem, The Netherlands) in ammonium bicarbonate (Ambic, LC-MS grade, 40,867, Merck, Darmstadt, Germany) 50 mM for 30 min at 65 °C and alkylated using 20 mM iodoacetamide (RPN6302V, GE Healthcare, Chicago, IL) in Ambic medium, 50 mM (Ambic, Witney, United Kingdom) for 30 min at 37 °C in the dark. Protein digestion was performed using sequencing grade trypsin (11,418,033,001, Roche, Indianapolis, IN) at a modified enzyme:protein ratio (*w*/w) of 1:50 for 17 h at 37 °C. Then the samples were incubated with 10% trifluoroacetic acid (LC-MS grade, 80,457, Sigma-Aldrich) for 10 min at 37 °C in a Thermomixer Compact at 500 rpm to quench the trypsin reaction and remove sodium deoxycholate by acid precipitation. After centrifugation for 10 min at 13000 rpm and 4 °C, the supernatants were desalted with Mobicol spin columns (M1003, Mo Bi Tec, Goettingen, Germany) equipped with 10 μm pore size filters (M2110, Mo Bi Tec), and transferred to a clean tube, which was filled with a C18 stationary phase (VersaFlash spherical C18 bonded flash silica, Supelco Analytical, Bellefonte, PA). The peptide mixtures were evaporated to dryness under vacuum at 36 °C (Speed Vac Concentrator, Savant Instruments Inc., Farmingdale, NY), before being resuspended in 50 μL of 5/95 CH_3CN/0.1% HCOOH to achieve a final peptide concentration of 2 μg/μL (acetonitrile, hypergrade for LC-MS LiChrosolv, Merck; and formic acid LC-MS grade, Merck). Finally, the samples were transferred into plastic vials for the subsequent LC-MS/MS analysis. All aqueous solutions were prepared using Milli-Q deionized water filtered on a Millipak filter (0.22 μm, MPGL040001) and purified on an LC-Pak cartridge (C18, LCPAK0001), all Millipore (Bedford, MA).

2.8.2. LC-MS/MS analysis

The analyses were performed using a micro-HPLC Eksigent Ekspert microLC 200 combined with a Triple TOF 5600 mass spectrometer equipped with a Turbo Ion Spray probe as the ion source (all AB Sciex, Framingham, MA). We adopted the approach used in our previous publication with some modifications (Di Giorgi et al., 2022). Five μL of each sample/pool vial, placed in an autosampler at 8 °C, was injected in triplicate onto a C18 Jupiter column (150 mm 0.3 mm, 4 μm particle size, 90 Å) thermostatted at 30 °C and equipped with a micro trap C18 (10 mm 0.3 mm) (both Phenomenex, Torrance, CA, USA). The flow rate was set at 5 μL/min and the mobile phases A and B were, respectively, H_2O and CH_3CN, both with 0.1% HCOOH. The elution program was: 0 min, 5% B; 1 min, 5% B; 51 min, 22% B; 51.5 min, 90% B; 53.5 min, 90% B; 54 min, 5% B; 60 min, 5% B. Chromatographic performances and TOF accuracy were evaluated using an intra-run injection (5 μL) of 100 fmol/μL beta-galactosidase-digested proteins (4,333,606, AB Sciex). The mass spectrometer was set in the positive ion mode, and the operating conditions of the ion source were the following: ion spray voltage floating, 5.5 kV, probe temperature, 150 °C, curtain gas, 25 psi, ion source gas 1 and gas 2, respectively 30 and 20 psi, declustering potential, 100 V. N_2, as an inert gas, was used for collision-induced dissociation (CID) experiments.

A sample pool was analyzed with an information-dependent acquisition (IDA) tandem mass spectrometry method based on an MS1 survey scan from which the 20 most abundant precursor ions were selected for subsequent CID fragmentation. The MS1 survey scans and MS2 scans were acquired over a mass range of 250–1250 *m/z* and 100–1500 *m/z*, with an accumulation time of 250 and 100 ms, respectively. CID experiments were carried out using rolling collision energies that were automatically calculated according to the *m/z* and the charge of the candidate ion, with a collision energy spread (CES) of 5 V. Precursor ions with a charge state ranging from 2^+ to 5^+ were chosen to trigger the MS/MS experiments. The isolation width for precursor ion selection was set at 0.7 *m/z* on the Q1.

IDA results were used to generate the SWATH data-independent acquisition (DIA) method for protein quantitation. For each sample, the SWATH acquisitions were performed over 50 overlapping isolation mass windows of variable length (minimum window width 3 Da, window overlap 1 Da) depending on the peptide density distribution along the entire mass range of 250–1250 *m/z*. Precursor ion activation was performed by CID, as described above, but an acquisition mass range of 230–1500 *m/z* and a charge state of 2^+ were chosen. An accumulation time of 100 ms for MS1 and 50 ms for MS2 scans resulted in an overall duty cycle of 2.6 s (~15 points per elution peak).

2.8.3. Data processing and analysis

SWATH data analysis was carried out with DIA-NN (https://github.com/vdemichev/DiaNN) version 1.8, the free universal software for DIA proteomics data processing by V. Demichev, M. Ralser, and K. S. Lilley (The Francis Crick Institute, Molecular Biology of Metabolism laboratory, London, UK and Department of Biochemistry and The Milner Therapeutics Institute, University of Cambridge, Cambridge, UK).

First, the SWATH raw file.wiff was converted into .wiff.dia and then used to generate the spectral library utilizing the following options: FASTA digest for library-free search/library generation, enabled; Zebrafish Swiss-Prot FASTA database of 3233 reviewed, non-redundant protein species (downloaded on 4 May 2022); deep learning-based spectra, RTs and IMs prediction, enabled; protease = trypsin; missed cleavages = 2; maximum number of variable modifications = 3; N-term M excision, C carbamidomethylation as fixed modification, and M oxidation as variable modification, all enabled; peptide length range = 7–30; precursor charge range = 1–4; precursor *m/z* range = 250–1250; fragment ion *m/z* range = 230–1500; generate spectral library, enabled; precursor FDR = 1%; mass accuracy was determined automatically (mass accuracy = 0, MS1 accuracy = 0); use isotopologues, MBR (match between run), and remove likely interferences, all enabled; neural network classifier = single-pass mode; protein inference = genes; quantification strategy = any LC (high accuracy); cross-run normalization = RT-dependent; library generation = smart profiling. Where not specified, the standard settings were used.

For the protein quantitation step on files.wiff.dia, we kept the same parameters used above for spectral library generation, with the following exceptions: in the spectral library, the report-lib.tsv file generated in the previous step was selected; the generate the spectral library, FASTA digest for library-free search/library generation and deep learning-based spectra, and RTs and IMs prediction options were all disabled; quantitative matrices were enabled.

The DIA-NN report-quantification.pg_matrix output file, reporting the $\log_2$ transformed cross-run normalized protein areas (obtained as the sum of the intensity of the top three precursor ions identified at 1% FDR and cross-run normalized), was used for the subsequent data analysis.

In order to identify the differentially expressed proteins (DEPs) between the *cln8*$^{-/-}$ and WT groups, a *p*-value <0.05 and FC 20% were selected. Filtered datasets of DEPs from both groups were evaluated by means of QIAGEN's Ingenuity Pathway Analysis (IPA Winter Release - December 2020; QIAGEN, Hilden, Germany), to identify meaningful biological processes and molecular pathways.

2.9. Live staining imaging

To visualize apoptotic cells, *in vivo* staining was carried out in live, PTU-treated, manually-dechorionated larvae at 24 hpf using the vital dye acridine orange (AO, #235474; Sigma-Aldrich). Zebrafish embryos were incubated with 10 μg/mL AO solution for 15 min in the dark; the larvae were then washed three times with E3 medium. LysoTracker Green DND-26 (L7528, Thermo Fisher Scientific; 1:1000) and BODIPY™ 493/503 (D3922, Thermo Fisher Scientific, 100 μM) were used to stain lysosomes and other acidic organelles and neutral lipids, respectively, in live zebrafish larvae. Zebrafish larvae at 5 dpf were incubated with the dye for 30 min in the dark. Following the staining, larvae were rinsed 3 times with fresh egg water. All images were acquired using a Leica M205FA stereo-microscope (Leica Microsystems), and fluorescence analysis was performed using Image-J software v.1.46, calculating the fluorescent intensity in the region of interest (ROI). All the ROIs used for the analysis were designed excluding the yolk/gut area and were localized in the brain (AO, Lysotracker and BODIPY), and in the body (Lysotracker).

2.10. Immunohistochemistry staining of whole-mount zebrafish embryos

To prevent the development of pigmentation, embryos were treated with 0.005% *N*-phenylthiourea (P7629; Sigma-Aldrich) from 24 hpf. Whole-mount immunohistochemistry was performed in 48 hpf or 120 hpf embryos fixed in 4% paraformaldehyde overnight at 4 °C and stored in methanol. The primary antibody used was anti-ATP synthase subunit C (SCMAS) antibody (ab181243; Abcam, Cambridge, UK1;100). Images were acquired using a Leica M205FA stereo-microscope (Leica Microsystems) with a ROI placed in the body.

2.11. Locomotor behavior

Coiling behavior was measured to assess burst activity in homozygous *cln8*$^{-/-}$ and WT embryos at 30 hpf; to this end, the number of tail flicks in 30 s was measured using a Leica M205FA stereo-microscope (Leica Microsystems) connected with Danioscope software (Noldus Information Technology). Larval locomotor behavior (distance traveled and velocity) was measured in homozygous *cln8*$^{-/-}$ F2 larvae and WT larvae at 5 dpf using the DanioVision device (Noldus Information Technology). Briefly, single larvae were transferred into 96-well plates containing 300 μL of E3 medium per well. Then, plates were placed, one at a time, in the DanioVision system, and larval locomotor activity was recorded for 30 min and analyzed using EthoVision XT software (Noldus Information Technology). Adult locomotor behavior was measured in homozygous *cln8*$^{-/-}$ and WT animals (12 months old, 50:50 male:female ratio) using the open field test, an assay commonly used to study animals' exploration and emotionality. The arena consists of a rectangular transparent tank (40 cm height × 40 cm width × 40 cm length) and behavioral tests were performed under light conditions using a top-view digital camera. At each trial, a single fish was gently placed in the center of the tank (filled with water of the same temperature as that of the home tank) and video-recorded for 5 min. The fish-test room was empty during the recording, to avoid disturbing the animals. All trials were analyzed using Ethovision XT17 video-tracking software (Noldus Information Technology), and distance traveled and velocity were measured.

2.12. Electroretinogram recording (ERG)

ERG was performed on zebrafish (both *cln8*$^{-/-}$ F2 and WT) at 5 dpf, 6 dpf, and 6 weeks post fertilization (Masek et al., 2023). A single eye of each individual fish was stimulated with flashes of 5 different light intensities, and the corresponding ERG b-wave amplitude was quantified.

2.13. Simultaneous local field potential (LFP) and calcium imaging recordings and statistical analysis

Electrophysiological forebrain recordings were performed in 120 hpf zebrafish larvae to characterize epilepsy phenotype. The larvae were placed on a drop of 1.2% low melting point agarose and LFPs were recorded with an AgCl electrode inside a glass micropipette back loaded with 2 M NaCl. Electrophysiological signals were amplified 500-fold (EXT-02F, NPI, Tamm, Germany), band pass filtered (0.3–1300 Hz), and digitized at a rate of 5 kHz (Axon Digidata 1550B, Clampex 10.7.0.3, Molecular Devices, Berkeley, CA). The microelectrode was positioned by advancing its tip until it punctured the skin, after which it was carefully advanced into the forebrain. Data analyses of the LFP recordings were performed using a suite of custom MATLAB scripts. Burst activity analysis was performed on the LFP signals filtered in the 30–95 Hz band as already described. The root mean square (RMS) power of the signal was computed on the recording on rolling windows of 250 ms and in steps of 50 ms. The distribution of the logarithm of the RMS power measurements was fitted with a single Gaussian distribution. In some recordings, the distribution was characterized by an asymmetry due to a high-energy population. Those distributions were fitted with double Gaussians, then the ROC curves and areas under the curves were calculated; values >0.9 were considered acceptable and events were extracted as described (Della Vecchia et al., 2022). For normally

distributed recordings, bursts were identified by extracting all events with a power higher than three standard deviations (SD) from the mean. Statistical analysis was performed using GraphPad Prism version 9 software (GraphPad Software Inc.). For the calcium imaging analysis, zebrafish larvae at 120 hpf were restrained in low melting point agarose and a Nikon FN1 microscope (Nikon, Tokyo, Japan) was used for video recording; the image acquisitions were obtained using a Prime sCMOS camera (Teledyne Photometrics, Tucson, AZ, USA) supplied with Metafluor software (Molecular Devices, San Jose, CA), applying a time-lapse interval of 150 ms and acquiring 3860 frames per video. The distribution of fluorescence fluctuations (DF/F0) in the brain area was evaluated in a pre-defined ROI using ImageJ 64 software. Data were normalized to background fluorescence and were quantified by the Pearson's coefficient of skewness defined as: $\sigma = (3(M–m))/\sigma$, where M is the mean, m is the median, and σ is the SD of the distribution, as described elsewhere (Cozzolino et al., 2020).

2.14. Pharmacological treatments

The molecules to be tested were first selected for their action as autophagy inducers from the SCREEN-WELL® Autophagy library (BML-28374) and, in preliminary experiments, were diluted to a final working concentration of 10 μM, using, as a carrier, DMSO at a final concentration of 0.01%. Other autophagy promoters were synthesized in Prof. Rapposelli's laboratory at the University of Pisa, in the manner already described elsewhere (Runfola et al., 2021; Chiellini et al., 2016). All the molecules were tested for their toxicity through evaluation of embryo morphology and death rate. Compounds found to be safe for embryo development or with no toxic effects derived from the use of DMSO as a carrier (Turner et al., 2012), were tested on *cln8*$^{-/-}$ mutants to verify possible rescue of locomotor defects. Finally, two more compounds after the first screen (trehalose and SG2) were selected for an in-depth analysis. Fifty 4 hpf embryos were randomly placed in 60 mm × 15 mm Petri dishes containing trehalose and SG2 diluted in egg water. Trehalose and SG2 stock solutions were prepared in Milli-Q water (Merck-Millipore, Milan, Italy) and diluted in egg water to final working concentrations of, respectively, 100 μM (Doccini et al., 2022) and 2.5 μM. The media were not refreshed during the experiment unless otherwise stated. To test treatment efficacy, we assessed tail coiling activity and performed locomotor behavioral assays, LFP and calcium recordings, qRT-PCR, and Western blotting.

2.15. Statistics

All data in the manuscript represent three or more independent experiments. Statistical analysis was performed using GraphPad Prism 6. All quantitative variables were analyzed using either parametric or non-parametric methods, depending on the distribution shown by the Shapiro-Wilk test. For comparisons between two different groups the analysis was performed using the *t*-test for normally distributed data; instead, the Mann-Whitney test was applied in the case of non-normally distributed data. For multiple comparisons, Dunn's test was performed after the Kruskal-Wallis test, since the data of the various groups examined did not show Gaussian distribution. Statistical significance is reported as follows: * $p \leq 0.05$, ** $p \leq 0.01$, *** $p \leq 0.001$, or **** $p \leq 0.0001$. The specific test applied for each analysis is reported in the figure legend.

3. Results

3.1. Spatiotemporal expression of cln8 in zebrafish

As already described the zebrafish cln8 protein is 289 amino acids long and has 54% identity with human CLN8 (Huber et al., 2020). We evaluated the spatiotemporal expression of *cln8* during zebrafish development. We found it to be expressed from the first stage of development (it is highly expressed at 0 hpf); after midblastula transition at 6 hpf its expression decreases and thereafter it is constantly expressed until 5 dpf. *In situ* hybridization of *cln8* mRNA revealed that it is expressed over the entire larval body at 5 dpf (Fig. 1A).

3.2. Generation of novel *cln8*$^{-/-}$ zebrafish line

We successfully edited the novel *cln8*$^{-/-}$ zebrafish model using the CRISPR/cas9 system, which resulted in an 11-bp deletion in exon 3 (Fig. 1B). This led to a frameshift mutation and an early stop codon in position 191 (Fig. 1C). The efficacy of the mutation was further confirmed by qRT-PCR analysis in homozygous F2 mutant *cln8*$^{-/-}$ larvae, which showed reduced expression of *cln8* mRNA *versus* control siblings (Fig. 1D). The reduced expression of *cln8* mRNA in *cln8*$^{-/-}$ mutant larvae might be due to nonsense-mediated mRNA decay (NMD). Moreover, we noted that this mutation did not affect viability, and indeed observed that the Mendelian ratios were maintained. We also observed no qualitative difference in phenotype between zygotic *cln8*$^{-/-}$ embryos derived from heterozygous females and maternal-zygotic (MZ) *cln8*$^{-/-}$ embryos obtained from homozygous *cln8*$^{-/-}$ females. This finding suggests that maternal *cln8* mRNA does not play a crucial role during early embryonic development in zebrafish. Morphological analyses of 5 dpf larvae showed that the *cln8*$^{-/-}$ mutant larvae had a slightly increased body length, a decreased eye size, and an increased yolk sac area (Fig. 1F).

3.3. Mutant *cln8*$^{-/-}$ zebrafish displayed impaired locomotor behaviors

Behavioral analyses performed at different stages of zebrafish development displayed increased tail coiling activity at 30 hpf (Fig. 2A) and locomotor defects at 5 dpf, as shown by a decreased distance traveled and decreased velocity compared with WT controls (Fig. 2B). Mutant embryos did not show typical increased locomotion associated with the onset of seizures. The locomotor defects of *cln8*$^{-/-}$ mutants were further confirmed in adulthood: mutant fish at 12 months showed altered swimming behavior (Fig. 2C).

3.4. *cln8*$^{-/-}$ larvae recapitulate the main pathological signatures of NCL

Compared with control larvae, *cln8*$^{-/-}$ larvae showed accumulation of SCMAS, a common hallmark of CLN8 disease (Fig. 3A). Moreover, using AO, we observed increased apoptosis in the brain at 24 hpf (Fig. 3B). The *cln8*$^{-/-}$ mutant larvae also showed decreased fluorescence after Lysotracker staining, possibly indicating lysosomal alkalization, as already described in CLN8-deficient cells (Fig. 3C) (Pesaola et al., 2021). Furthermore, our mutants showed an accumulation of neutral lipids compared with the WT controls (Fig. 3D). Mass spectrometry-based proteomic analysis of 5 dpf whole larvae quantified 279 proteins. We identified 15 DEPs between *cln8*$^{-/-}$ and WT larvae with a *p*-value <0.05 and FC >20% (**Supplementary Table 2**). It is worth noting that the limited number of DEPs in our study is due to a reduced annotation of the zebrafish proteome (Chodkowski et al., 2023). DEPs were sorted on the basis of their interconnectedness and prediction of the upstream or downstream effects of their activation or inhibition. We constructed two distinct networks of molecules predicted to be involved in *Developmental Disorders*, *Hereditary Disorders*, and *Lipid Metabolism* (network 1 – score 24; number of focus molecules, 9) and *Cell Morphology*, *Cell Compromise* and *Molecular Transport* (network 2 – score 15; number of focus molecules, 6), respectively (**Supplementary Figs. 1 A-B**). We examined the overlap of molecules belonging to the considered disease categories (**Supplementary Fig. 1C**) and, among others, we identified the npc2 protein, which was particularly overexpressed. To validate proteomic data, we assessed the mRNA expression of two DEPs (mRNA levels of *sept3* and *ddi2*) and confirmed their downregulation in mutant larvae as compared to control siblings (**Supplementary Fig. 1D**).

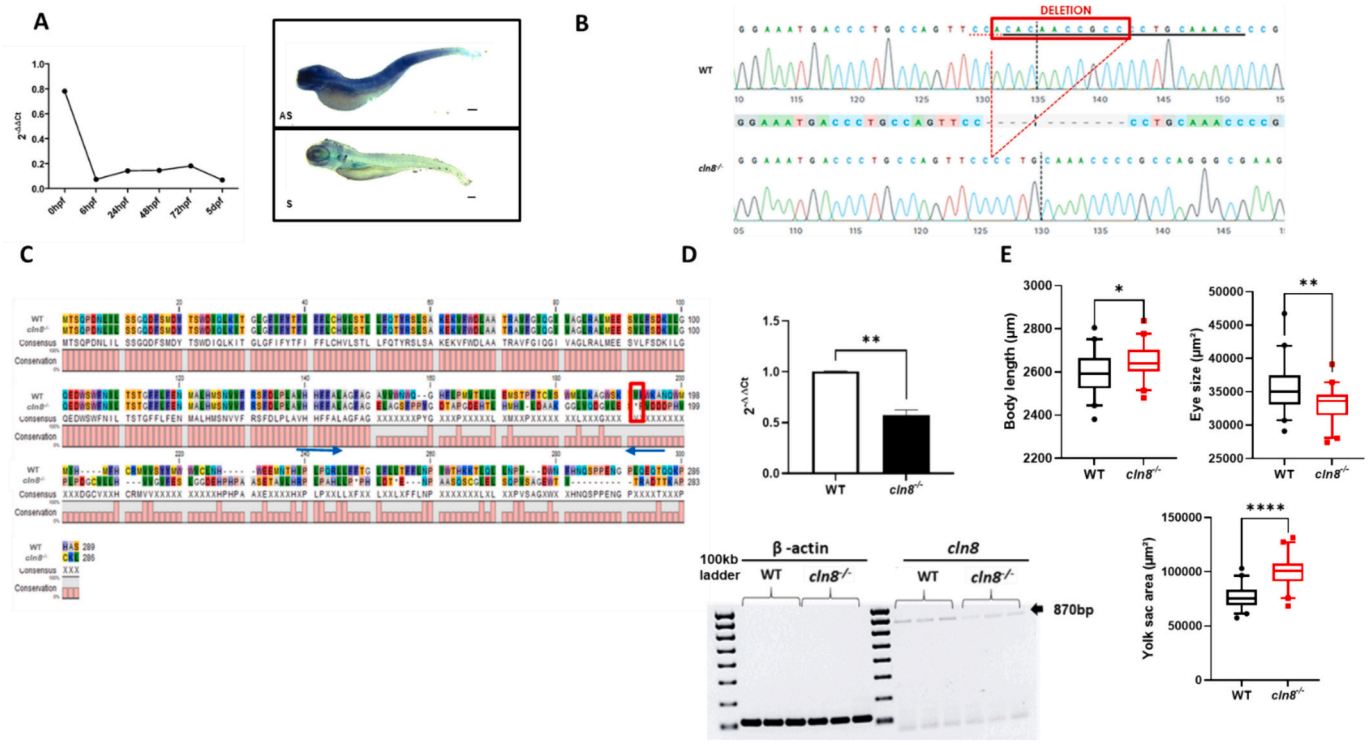

Fig. 1. Generation of *cln8*$^{-/-}$ mutants.
(A) Temporal and spatial expression of *cln8* mRNA during zebrafish development evaluated using qRT-PCR and *in situ* hybridization at 5 dpf, the upper image indicates the antisense probe (AS), the figure below is the sense probe (S). **(B)** Sequence alignment of WT and mutant *cln8*$^{-/-}$ embryos shows the generation of *cln8*$^{-/-}$ mutant zebrafish by deletion of 11 bp of the *cln8* gene. **(C)** Protein alignment of WT and mutant *cln8*$^{-/-}$. The red rectangle shows the premature stop codon at residue 191 (p.Ala151Glufs*191), while the blue arrows indicate the forward and reverse primers used for qRT-PCR. **(D)** qRT-PCR analysis revealed a decrease in *cln8* mRNA expression, normalized to *β-actin*. The image represents the RT-PCR of of the entire *cln8* coding sequence, showing the decreased expression in mutants. Three independent RNA samples (each obtained from about 30–40 larvae) from *cln8*$^{-/-}$ larvae at 120 hpf and from controls were analyzed. The values are expressed as mean ± standard deviation (SD). $^{**}p \leq 0.05$, calculated by Student's *t*-test. **(E)** Morphology analysis of 5 dpf *cln8*$^{-/-}$ and WT embryos shows a slight increase in body length, a decreased eye size and an increased yolk sac area in the mutant larvae ($n = 40$). Data are represented as box and whisker plot with 5–95% confidence interval. All data were obtained from three independent experiments and were analyzed through statistical analysis ($^{***}p \leq 0.001$; $^{*}p \leq 0.05$) performed using the Mann-Whitney test.

3.5. Mutants displayed normal visual responses to light stimuli

In order to verify the impairment of the visual system in zebrafish *cln8*$^{-/-}$ larvae, we performed ERG recordings. The zebrafish ERG response is dominated by the ERG b-wave, which represents the depolarization of ON bipolar cells in response to light (Zang and Neuhauss, 2021). The results of our tests revealed decreased b-wave amplitudes in *cln8*$^{-/-}$ mutants compared with WT siblings at 5 dpf, but not at 6 dpf or at 6 weeks post fertilization (**Supplementary Fig. 2**), which indicates that the defect observed at 5 dpf might be due to the smaller size of the eyes at that time point (Fig. 1F). Overall, *cln8*$^{-/-}$ mutants showed normal visual function from 6 dpf on.

3.6. Identification of seizure-like events in the brains of *cln8*$^{-/-}$ larvae

Simultaneous forebrain LFP recordings and brain calcium imaging were performed on WT and *cln8*$^{-/-}$ larvae at 5 dpf in order to identify seizure-like events. We observed altered brain activity in mutant compared with control larvae (Fig. 4A). Statistical analysis of LFP recordings confirmed the presence of seizure-like events in *cln8*$^{-/-}$ larvae, showing increased duration and power of the detected events (Fig. 4B). These data were further confirmed through statistical analysis of the calcium imaging, which revealed increased skewness, suggestive of recurrent large fluctuations of intracellular Ca^{2+} (Fig. 4C), nicely reflecting the observations based on the LFP statistics.

3.7. Increased inflammation was associated with cln8 defects

Assessment of expression of genes involved in the inflammatory pathway revealed increased expression of some of the key factors such as the cytokines *tnfα* (tumor necrosis factor alpha) and *il-1β* (interleukin-1 beta), indicating increased inflammation in *cln8*$^{-/-}$ larvae (Fig. 5) (Yuan et al., 2022).

3.8. Impaired autophagy in *cln8*$^{-/-}$ larvae

We performed gene and protein expression analyses of different factors involved in the autophagy pathway. Several markers, namely *mTOR, beclin, atg5, lc3b,* and *atg12,* were found to be upregulated in *cln8*$^{-/-}$ larvae, whereas other factors (*lc3a, p62* and *tfeb*) showed normal expression (Fig. 6A). Expression of hypoxia-inducible factor-1α (*hif-1α*) was downregulated in *cln8*$^{-/-}$ compared with control siblings (Fig. 6A). Western blotting analyses revealed that *cln8*$^{-/-}$ mutants expressed higher a LC3II/LC3I ratio and higher Rab7 and cathepsin D (CTSD) levels, whereas levels of ATG5 were normal (Fig. 6B).

3.9. Potential beneficial effects of two pro-autophagy molecules

We screened 22 molecules known to be autophagy promoters; some of them are already FDA approved and others are original molecules (personal communication from our co-author Sim. R.; Runfola et al., 2021; Chiellini et al., 2016). Compounds that showed a toxic effect on morphology or caused an increased death rate were discarded. The

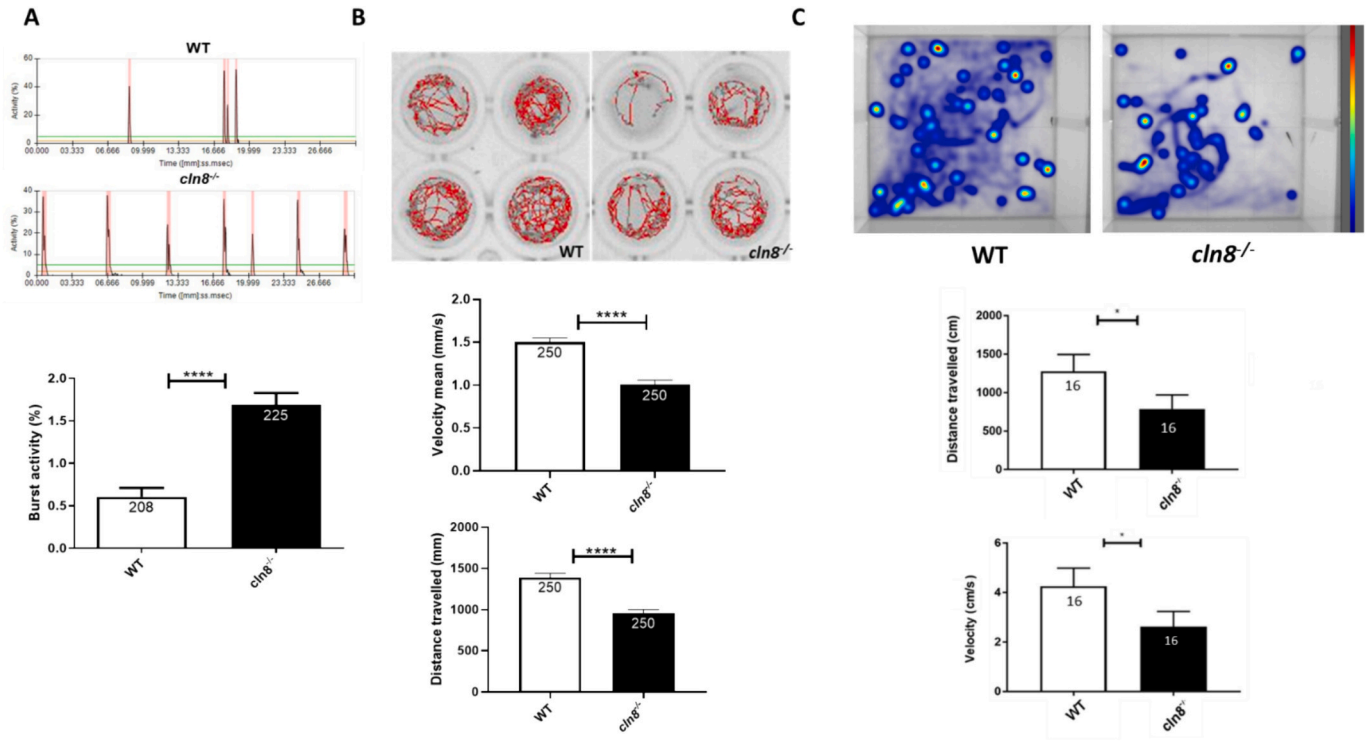

Fig. 2. Characterization of locomotor behavior of *cln8*$^{-/-}$ mutants.
(A) Analysis of coiling behavior (tail flicks) in 30 hpf WT and *cln8*$^{-/-}$ mutant embryos. **(B)** Locomotion analysis of 5 dpf WT and *cln8*$^{-/-}$ larvae. **(C)** Locomotor behavior of adult WT and *cln8*$^{-/-}$ zebrafish. All data were obtained from three independent experiments and were analyzed through statistical analysis (***p ≤ 0.001; *p ≤ 0.05) performed using the Mann-Whitney test. The values are expressed as mean ± standard error of the mean (SEM).

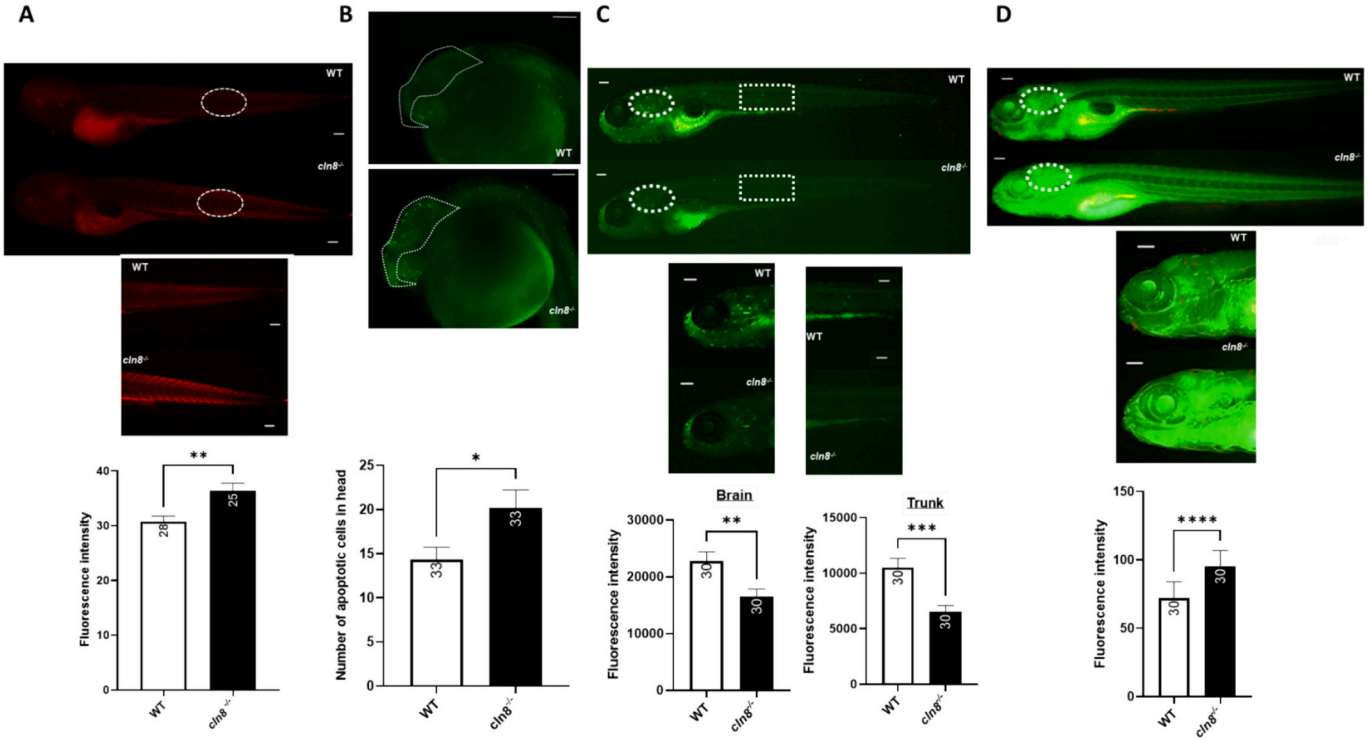

Fig. 3. Evaluation of the pathological signs of NCL in *cln8*$^{-/-}$ mutants.
(A) Immunofluorescence analysis of subunit c of mitochondrial ATP synthase (SCMAS) in 5 dpf WT and *cln8*$^{-/-}$embryos. **(B)** Acridine orange staining in brains of mutant and control 24 hpf embryos. **(C)** Lysotracker *in vivo* staining in 5 dpf WT and *cln8*$^{-/-}$ larvae. **(D)** Bodipy staining in live 5 dpf mutant and control larvae. Three independent experiments were performed in each group: *cln8*$^{-/-}$ and controls. Statistical analysis was performed using the Mann-Whitney test (****$p \leq 0.0001$; ***$p \leq 0.001$; *$p \leq 0.05$). (scale bar = 100 μm). The number inside the bars is the sample size. The values are expressed as mean ± standard error of the mean (SEM).

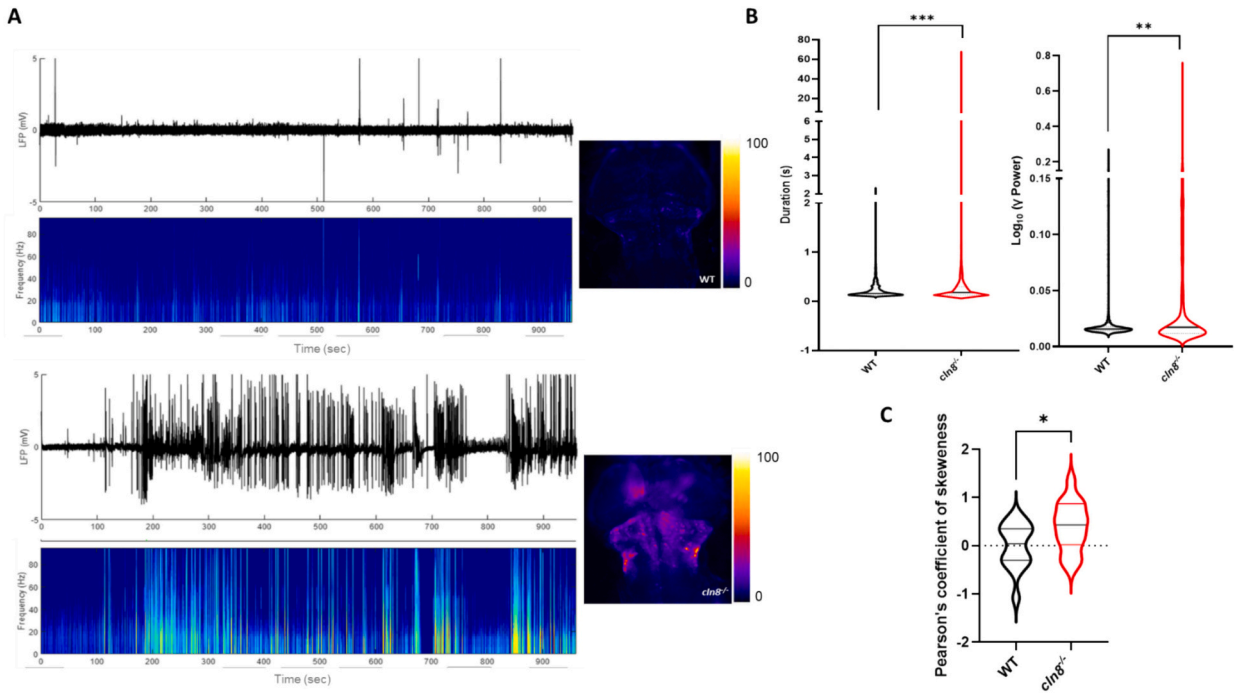

Fig. 4. Electroencephalographic recordings and brain calcium imaging in *cln8*$^{-/-}$ mutants.
(A) The images on the left show the local field potential (LFP) traces of 5 dpf WT and *cln8*$^{-/-}$ larvae with (below) the power spectrum calculated in the 30–95 Hz passband lasting 16 min. On the right, the representative z-projection images of the brain calcium imaging performed in the larvae in 16 min of recording (see calcium fluorescence heatmap). **(B)** LFP analysis using MATLAB software. The graphs represent the duration and power of identified events in 15 WT and 15 *cln8*$^{-/-}$ fish. **(C)** Analysis of calcium imaging was performed by calculating Pearson's coefficient of skewness in the two groups. Statistical analysis was performed using the Mann-Whitney test (****$p \leq 0.0001$; ***$p \leq 0.001$; **$p \leq 0.01$; *$p \leq 0.05$). Violin plots show the median and quartiles.

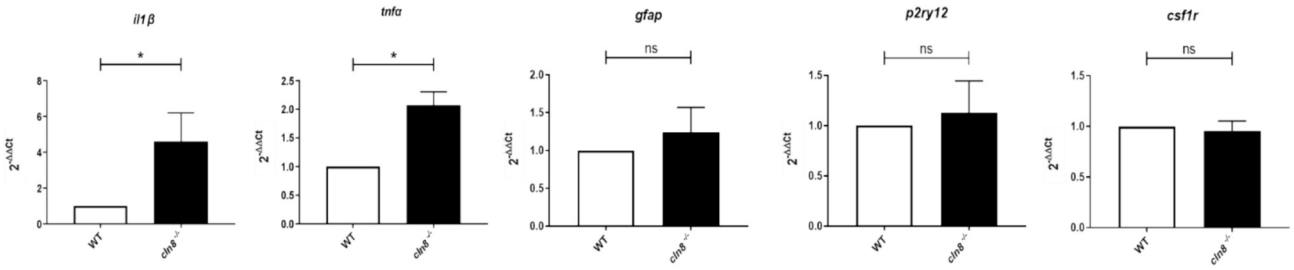

Fig. 5. Evaluation of inflammatory response in cln8$^{-/-}$ mutant larvae.
qRT-PCR analysis of inflammatory factors. Three independent experiments were performed for each experimental group (*cln8*$^{-/--}$ and WT controls). Statistical analysis (*p $\leq$ 0.05) was performed using the *t*-test. The values are expressed as mean ± standard error of the mean (SEM).

corresponding author can be contacted for the full list. After the toxicological analyses, five molecules were selected to be tested on *cln8*$^{-/-}$ larvae to verify their locomotor effects at 5 dpf (**Supplementary Table 3 and Supplementary Fig. 3**). However, we observed a hyperactive locomotor behavior both in WT and *cln8*$^{-/-}$ caused by the treatment with the vehicle, DMSO, at a concentration of 0.01% a finding already reported by others (Huang et al., 2018; Christou et al., 2020; Turner et al., 2012). Thus, we decided to focus our studies only on those molecules dissolved in fish water. Only two molecules (trehalose and SG2) were selected for in-depth characterization. Both trehalose and SG2 were able to rescue the behavioral defects, as shown by an increase in the distance traveled by the treated *cln8*$^{-/-}$ larvae as well as in their velocity, even though those larvae failed to reach the values achieved by their WT siblings (Fig. 7A). The two compounds were able to decrease burst activity in treated *cln8*$^{-/-}$ embryos compared with untreated ones (Fig. 7B). Indeed, SG2 was able to reduce both the duration and power of seizure-like events in *cln8*$^{-/-}$ mutants, whereas trehalose slightly reduced only their duration (Fig. 7C), while waves of calcium spreading were not affected by the treatments (Fig. 7D). It is important to say that prior to these tests we had verified the presence of similar levels of trehalase expression in both mutant and WT embryos. In humans and mice, too, trehalase can specifically bind and hydrolyze trehalose, and it is critical for the mechanism of action of this compound (**Supplementary Fig. 4**).

Finally, we observed that both compounds increased the expression of *hif-1α*) (Fig. 8A). Only SG2 reduced the LC3II/LC3I ratio (Fig. 8B) and only trehalose reduced expression levels of Rab7 and CTSD (Fig. 8C).

4. Discussion

In an effort to bridge the gap between cell and mammalian models for pilot drug screening in CLN8 dysfunction, we created a novel zebrafish model of NCL. The generated maternal zygotic *cln8*$^{-/-}$ mutants showed decreased transcript levels as demonstrated by real-time PCR analysis and RT-PCR amplification of the whole coding sequence of the *cln8* zebrafish gene; this might be a consequence of the NMD

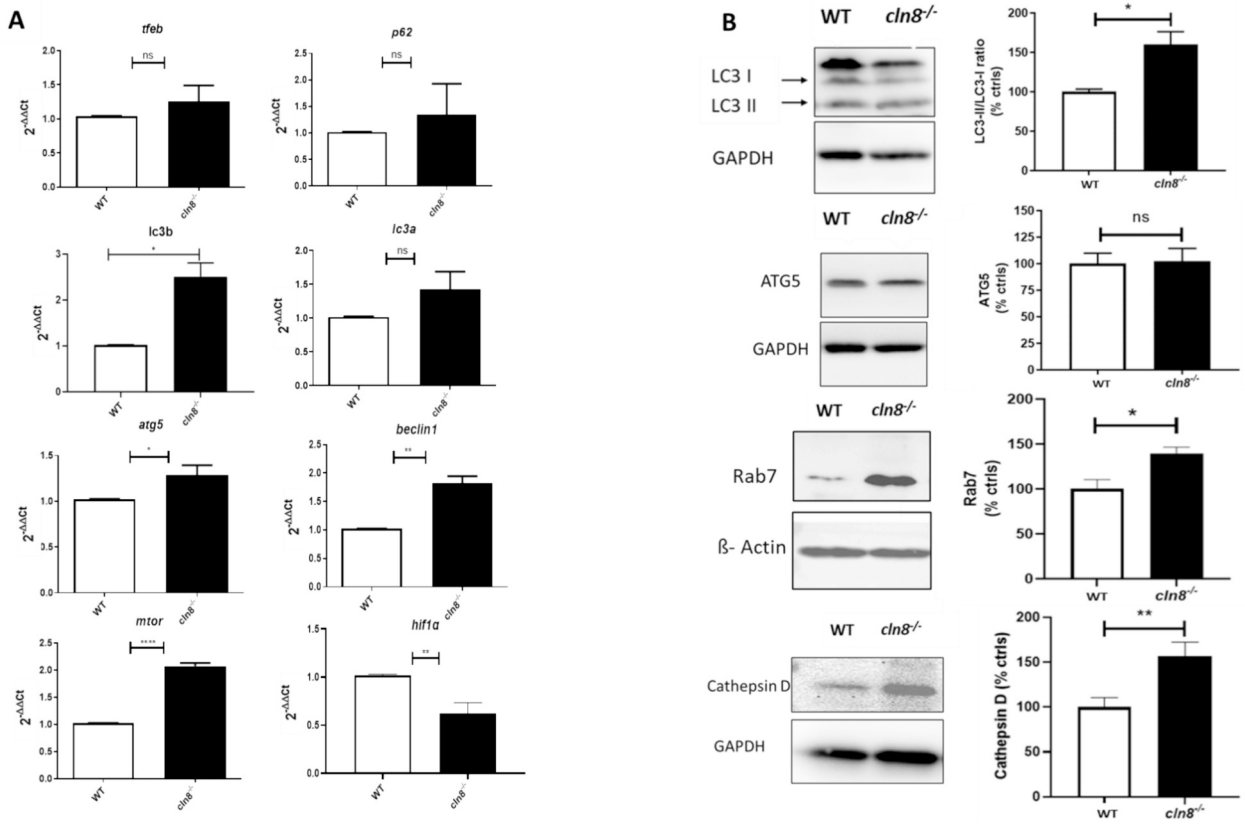

Fig. 6. Analysis of autophagy pathway in *cln8*$^{-/-}$ mutants.
(A) The graphs show the qRT-PCR analysis of autophagy factors, performed by normalizing to *β-actin*, and comparing *cln8*$^{-/-}$ larvae with controls at 5 dpf. Three independent samples (each obtained from about 30–40 larvae) from controls and *cln8*$^{-/-}$ mutant larvae at 120 hpf were analyzed. Statistical analysis (* $p \leq 0.05$, **$p \leq 0.01$, *** $p \leq 0.001$) was performed using Student's t-test. The values are expressed as mean ± standard deviation (SD). **(B)** Three independent larval homogenates from controls ($n = 50$) and *cln8*$^{-/-}$ larvae (n = 50) were tested by Western blotting for the expression of LC3, Rab7, Ctsd, and ATG5 protein. The levels of the proteins were normalized to ß-actin or GAPDH. Statistical analysis (*$p \leq 0.05$, **$p \leq 0.01$) was performed using Student's t-test. The values are expressed as mean ± standard error of the mean (SEM).

mechanism which might induce a decreased protein level. It should be noted that we did not characterize the zygotic *cln8*$^{-/-}$mutants which may have a milder phenotype due to the presence of maternal *cln8* mRNA in the early stages of the embryogenesis. This novel mutant recapitulates several of the characteristics of NCL disease, including impaired locomotion (perhaps correlating with an ataxic phenotype) and a clear seizure-prone ("epileptic") phenotype, common to CLN8 patients but not seen in *mnd* mice (Kolikova et al., 2011). Furthermore, the inflammatory response in our *cln8*$^{-/-}$ mutants was already activated in the early stages of embryogenesis, as also observed in the *mnd* mouse which is reported to show integration of ER stress pathways with an increased inflammatory response in CNS structures (Galizzi et al., 2011). Overall, characterization of this new *in vivo* model showed that it recapitulates at least some of the main pathological signatures of NCL disease.

In vivo exploration of CLN8 disease has shown the protein dysfunction to lead not only to impaired lysosomal biogenesis, but also to enhanced lipid accumulation and impaired autophagy (Kim et al., 2022). The increased levels of the autophagosome marker (LC3II) and of a late endosome marker (Rab7) suggest impairment of the autophagy pathway, which may indicate decreased autophagosome-lysosome fusion, with consequent accumulation of these two proteins. We also observed increased expression of CTSD, whose over-secretion is reported in mouse models of other NCL forms (Bartsch et al., 2013; Wavre-Shapton et al., 2015). Reduced expression of CTSD in CLN8 KO cells, observed in another study (di Ronza et al., 2018), may be due to the different analysis performed, *i.e.*, whole larval body (present work) *versus* lysosome-enriched fractions (di Ronza et al., 2018), or to unanticipated differences between fish and humans.

In the present study, we were able to investigate, for the first time, proteomic profiles in a zebrafish model of NCL. These profiles in fish larvae were found to strongly corroborate the aforementioned evidence of impaired lipid metabolism and impairment of the autophagy pathway, although several proteins directly involved in the autophagy pathway were not identified with our assay, probably because of the reduced annotation of the zebrafish proteome (Chodkowski et al., 2023) or the extremely stringent bioinformatic setting in our study. Nonetheless, NPC2, found to be upregulated in our system, was also increased in cortical neurons from patients with CLN3 disease (Chear et al., 2022); furthermore, its increased expression is associated with lysosomal accumulation of cholesterol (Li et al., 2015). Downregulation of *sept3* and *ddi2*, on the other hand, has been associated with sensing autophagy in neurons (Tóth et al., 2022) and with proteasome inhibition (Dirac-Svejstrup et al., 2020), respectively. These results confirm that autophagy is impacted by CLN8 dysfunction.

On these bases, we previously exploited a number of pro-autophagy compounds synthesized in house to investigate models of Alzheimer's disease (Runfola et al., 2021), and here used commercial FDA-approved libraries of compounds known to modulate autophagy. This was a proof-of-principle investigation designed to show that modulation of autophagy might rescue behavioral and molecular defects in *cln8*$^{-/-}$ larvae.

Our research identified two compounds that seem to be safe and capable of significantly reducing the power and the duration of the seizure-like events, although they did not rescue abnormal spread of

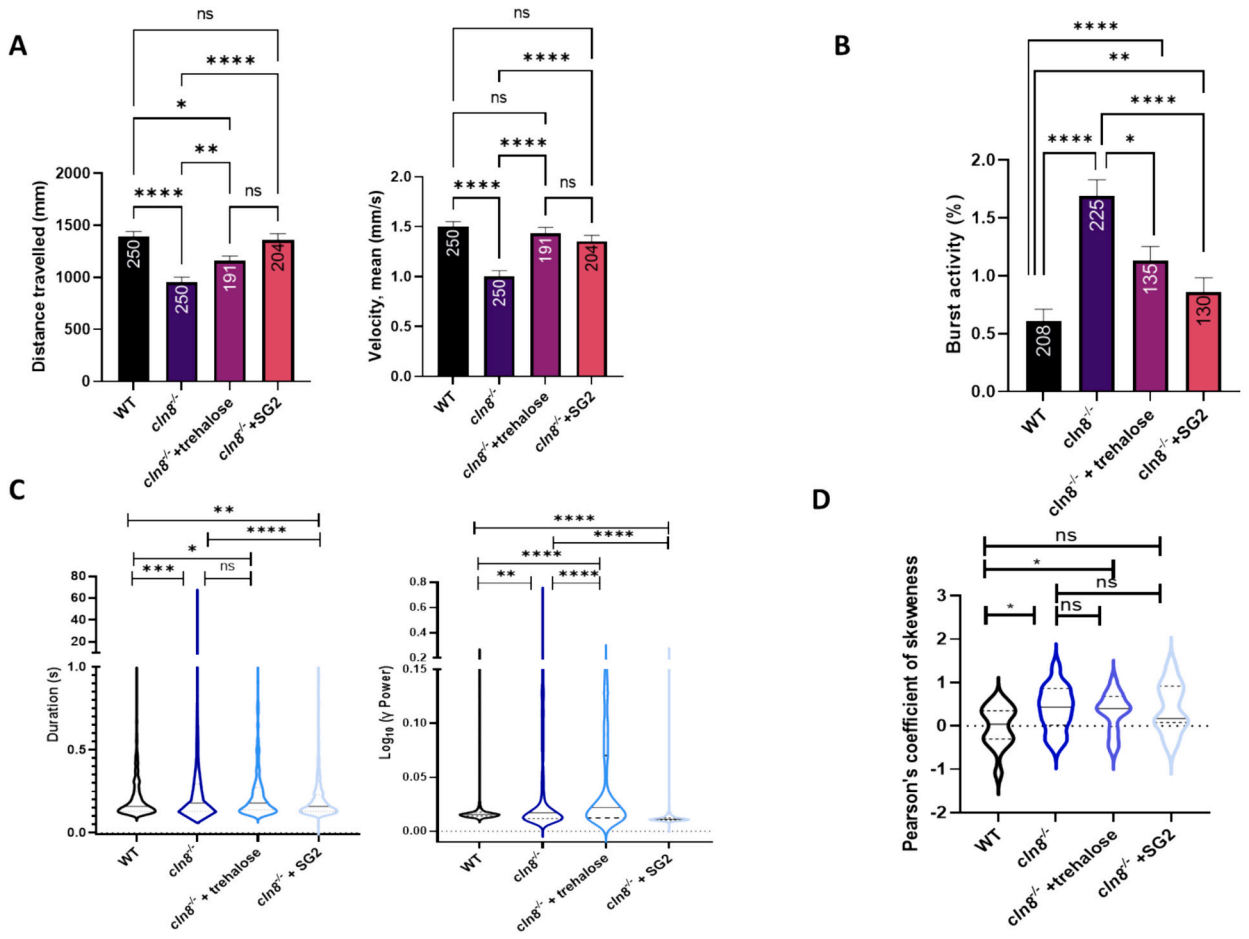

Fig. 7. Consequences of the effective molecules, SG2 and trehalose.
(A) Analysis of the effects of the SG2 and trehalose on locomotion (distance traveled and velocity) in *cln8*$^{-/-}$. **(B)** Analysis of the effects of the two compounds on coiling behavior of *cln8*$^{-/-}$ embryos. The values are expressed as mean ± standard error of the mean (SEM). **(C)** Analysis of the effects of trehalose and SG2 on the duration and power of LFP events. **(D)** Analysis of calcium imaging analysis performed by calculating Pearson's coefficient in WT and treated and untreated *cln8*$^{-/-}$. The experiments were performed in triplicate. The graphs represent the median and SEM. Statistical analysis (**** $p \leq 0.0001$; ***$p \leq 0.001$; **$p \leq 0.01$; *$p \leq 0.05$) was performed using the Mann-Whitney test. Violin plots show the median and quartiles.

cerebral calcium homeostasis.

It is important to highlight that both compounds allow increased expression of *hif-1α*, which is known to modulate autophagy and the underlying molecular mechanisms regulating this process (Wang et al., 2017). Moreover, trehalose seems to increase the LC3II/LC3I ratio and decrease Rab7 and CTSD expression compared with SG2, which may indicate that it exerts its effect by activating the lysosome and autophagosome biogenesis pathways. Trehalose is already known to have an anti-inflammatory effect and to activate lysosome and autophagosome biogenesis through the activities of TFEB and FOXO1 (Pupyshev et al., 2022).

SG2, on the other hand, is a member of a new class of synthetic diphenylmethane thyronamine analogs (Chiellini et al., 2015) whose mechanism of action has been found to produce a time-dependent recovery of autophagic activity in U87MG cells, due to downregulation of mTOR (Bellusci et al., 2017). Additionally, SG2 is able to modulate lipid metabolism through modulation of the AMPK/ACC pathway (Rogowski et al., 2019). However, the molecular mechanism underlying the multitarget effects of this novel drug candidate is currently under investigation. The multiple, divergent or similar roles of the two classes of compounds investigated here might favor their role in neurodegenerative conditions such as progressive myoclonic epilepsies similar to NCLs or other disorders characterized by impairment of autophagy, such as Alzheimer's disease and Parkinson's disease.

In summary, this study offers a novel CLN8 research tool that recapitulates much of the pathological phenotype of the human disease, and facilitates *in vivo* dissection of complex cellular pathways and high-throughput drug screenings. Further analysis of the fish mutants linked, for the first time, CLN8 dysfunction during development to impairment of autophagy. This enabled us to monitor the rescue effects of two interesting drugs.

5. Conclusions

While recapitulating many aspects of the human pathology, *cln8*$^{-/-}$ mutants pave the way for high-throughput screening of drugs, particularly those able to counteract dysregulated autophagy. Targeting autophagy, even during the years leading up to the emergence of gene therapy approaches, might offer new options for treating the human disease.

Funding

This work was partially supported by the Italian Ministry of Health (Ricerca Finalizzata SG-2018-12367839 to M.M.; Ricerca Corrente 2023, RC 5 × 1000 to M.M., S.D. and F.M.S); the Telethon Foundation (grants GSA23C003 and GGP20011 to M.M.), and Regione Toscana (Bando Ricerca Salute 2018, project DEM AGING to F.M.S.). M.M. is the holder of the Telethon Career Award.

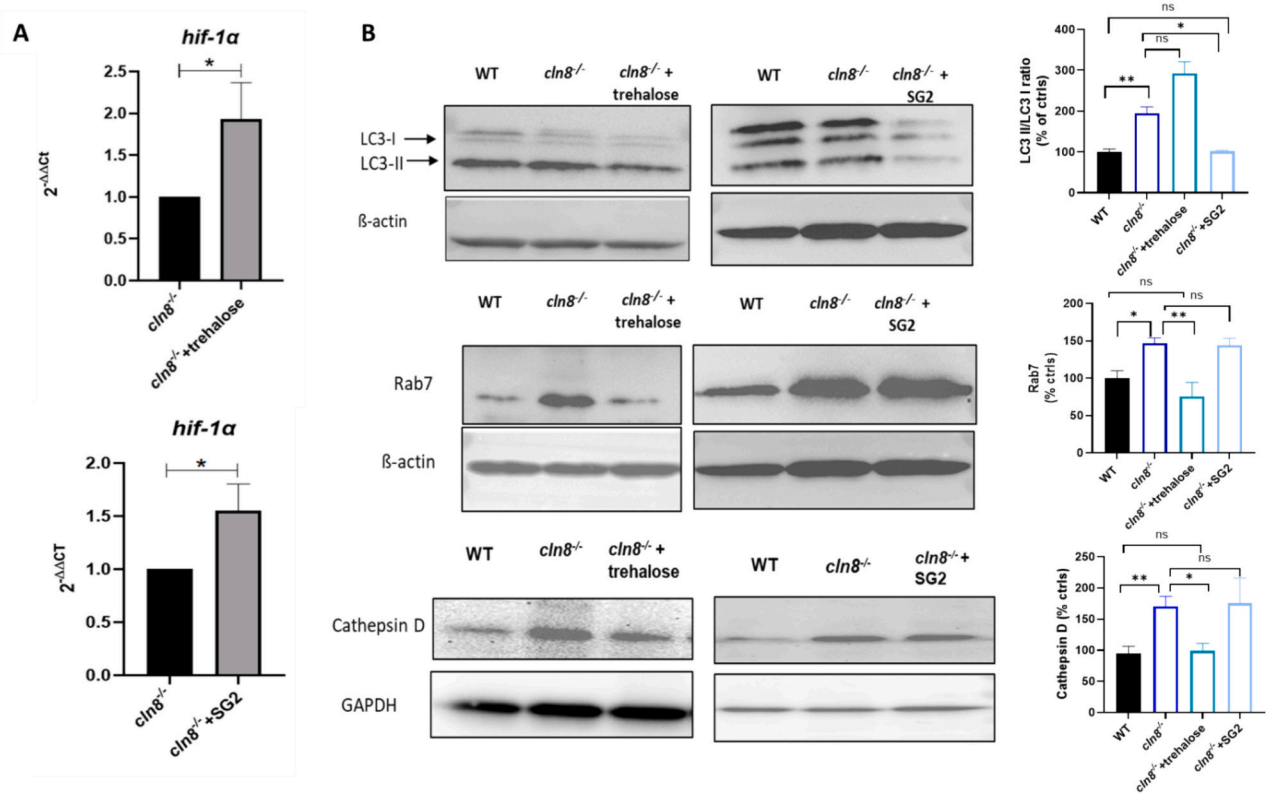

Fig. 8. Analysis of autophagy pathway after trehalose and SG2 administration.
qRT-PCR analysis of hypoxia-inducible factor 1-alpha (*hif-1α*). qRT-PCR analysis was performed (normalizing to β-actin) in untreated *cln8*$^{-/-}$ larvae compared with *cln8*$^{-/-}$ larvae treated with trehalose and SG2 at 5 dpf. Three independent RNA samples (each obtained from about 30–40 larvae) from controls and *cln8*$^{-/-}$ mutant larvae at 5 dpf 120 hpf were analyzed. *p ≤ 0.05, **p ≤ 0.01, ***p ≤ 0.001, calculated by Student's *t*-test. The values are expressed as mean ± standard error of the mean (SEM). **(B)** Three independent larval homogenates from WT ($n = 50$), untreated *cln8*$^{-/-}$ (n = 50) and treated *cln8*$^{-/-}$larvae were tested by Western blotting for the expression of LC3, Rab7 and cathepsin D protein. The levels of the protein were normalized to β-actin. * p ≤ 0.05, **p ≤ 0.01, calculated by one-way ANOVA test. The values are expressed as mean ± SEM.

Ethics approval

The current study does not involve human samples. All animal procedures were approved by the University of Pisa Animal Ethics Committee, and by the Italian Ministry of Health (approval n° n°584/2019-PR).

CRediT authorship contribution statement

Maria Marchese: Writing – review & editing, Writing – original draft, Visualization, Validation, Supervision, Software, Resources, Project administration, Methodology, Investigation, Funding acquisition, Formal analysis, Data curation, Conceptualization. **Sara Bernardi:** Writing – review & editing, Visualization, Methodology, Investigation, Formal analysis, Data curation. **Asahi Ogi:** Visualization, Methodology. **Rosario Licitra:** Visualization, Methodology. **Giada Silvi:** Visualization, Methodology. **Serena Mero:** Visualization, Methodology. **Daniele Galatolo:** Visualization, Methodology. **Nicola Gammaldi:** Visualization, Methodology. **Stefano Doccini:** Visualization, Formal analysis. **Gian Michele Ratto:** Visualization, Software. **Simona Rapposelli:** Visualization. **Stephan C.F. Neuhauss:** Visualization. **Jingjing Zang:** Visualization, Methodology. **Silvia Rocchiccioli:** Visualization. **Elena Michelucci:** Visualization, Methodology. **Elisa Ceccherini:** Methodology. **Filippo M. Santorelli:** Writing – review & editing, Visualization, Supervision, Funding acquisition, Conceptualization.

Declaration of competing interest

The authors declare that they have no conflicts of interest.

Data availability

All data are available within this manuscript, and raw data are available from the corresponding author upon reasonable request. Materials generated in this study are available from the corresponding author on request.

Acknowledgements

We are grateful to Dr. Baldassare Fronte of the University of Pisa for his technical support in the management of the zebrafish facility. We also thank Claire Wyart of the Institut du Cerveau et de la Moelle Épinière, Paris, France for providing the transgenic line Tg(neurod1: GCaMP6F). We thank Dr. Catherine J. Wrenn for language and editorial assistance. The authors thank the Italian patients' association (A-NCL) for their constant encouragement and support.

Appendix A. Supplementary data

Supplementary data to this article can be found online at https://doi.org/10.1016/j.nbd.2024.106536.

References

Adhikari, B., De Silva, B., Molina, J.A., Allen, A., Peck, S.H., Lee, S.Y., 2019. Neuronal ceroid lipofuscinosis related ER membrane protein CLN8 regulates PP2A activity and ceramide levels. Biochim. Biophys. Acta Mol. basis Dis. 1865 (2), 322–328. https://doi.org/10.1016/j.bbadis.2018.11.011.

Bartsch, U., Galliciotti, G., Jofre, G.F., Jankowiak, W., Hagel, C., Braulke, T., 2013. Apoptotic photoreceptor loss and altered expression of lysosomal proteins in the nclf

mouse model of neuronal ceroid lipofuscinosis. Invest. Ophthalmol. Vis. Sci. 54 (10), 6952–6959. https://doi.org/10.1167/iovs.13-12945.
Bellusci, L., Laurino, A., Sabatini, M., Sestito, S., Lenzi, P., Raimondi, L., Rapposelli, S., Biagioni, F., Fornai, F., Salvetti, A., Rossi, L., Zucchi, R., Chiellini, G., 2017. New insights into the potential roles of 3-iodothyronamine (T1AM) and newly developed thyronamine-like TAAR1 agonists in neuroprotection. Front. Pharmacol. 8, 905. https://doi.org/10.3389/fphar.2017.00905.
Bolivar, V.J., Scott Ganus, J., Messer, A., 2002. The development of behavioral abnormalities in the motor neuron degeneration (mnd) mouse. Brain Res. 937 (1–2), 74–82. https://doi.org/10.1016/s0006-8993(02)02470-8.
Bronson, R.T., Lake, B.D., Cook, S., Taylor, S., Davisson, M.T., 1993. Motor neuron degeneration of mice is a model of neuronal ceroid lipofuscinosis (Batten's disease). Ann. Neurol. 33 (4), 381–385. https://doi.org/10.1002/ana.410330408.
Chear, S., Perry, S., Wilson, R., Bindoff, A., Talbot, J., Ware, T.L., Grubman, A., Vickers, J.C., Pébay, A., Ruddle, J.B., King, A.E., Hewitt, A.W., Cook, A.L., 2022. Lysosomal alterations and decreased electrophysiological activity in CLN3 disease patient-derived cortical neurons. Dis. Model. Mech. 15 (12), dmm049651 https://doi.org/10.1242/dmm.049651.
Chiellini, G., Nesi, G., Digiacomo, M., Malvasi, R., Espinoza, S., Sabatini, M., Frascarelli, S., Laurino, A., Cichero, E., Macchia, M., Gainetdinov, R.R., Fossa, P., Raimondi, L., Zucchi, R., Rapposelli, S., 2015. Design, synthesis, and evaluation of thyronamine analogues as novel potent mouse trace amine associated receptor 1 (mTAAR1) agonists. J. Med. Chem. 58 (12), 5096–5107. https://doi.org/10.1021/acs.jmedchem.5b00526.
Chiellini, G., Nesi, G., Sestito, S., Chiarugi, S., Runfola, M., Espinoza, S., Sabatini, M., Bellusci, L., Laurino, A., Cichero, E., Gainetdinov, R.R., Fossa, P., Raimondi, L., Zucchi, R., Rapposelli, S., 2016. Hit-to-Lead optimization of mouse trace amine associated receptor 1 (mTAAR1) agonists with a diphenylmethane-scaffold: design, synthesis, and biological study. J. Med. Chem. 59 (21), 9825–9836. https://doi.org/10.1021/acs.jmedchem.6b01092.
Chodkowski, M., Zielezinski, A., Anbalagan, S., 2023. A ligand-receptor interactome atlas of the zebrafish. iScience 26 (8), 107309. https://doi.org/10.1016/j.isci.2023.107309.
Christou, M., Kavaliauskis, A., Ropstad, E., Fraser, T.W.K., 2020. DMSO effects larval zebrafish (*Danio rerio*) behavior, with additive and interaction effects when combined with positive controls. Sci. Total Environ. 709, 134490 https://doi.org/10.1016/j.scitotenv.2019.134490.
Cozzolino, O., Sicca, F., Paoli, E., Trovato, F., Santorelli, F.M., Ratto, G.M., Marchese, M., 2020. Evolution of epileptiform activity in zebrafish by statistical-based integration of electrophysiology and 2-photon Ca2+ imaging. Cells 9 (3), 769. https://doi.org/10.3390/cells9030769.
Della Vecchia, S., Ogi, A., Licitra, R., Abramo, F., Nardi, G., Mero, S., Landi, S., Battini, R., Sicca, F., Ratto, G.M., Santorelli, F.M., Marchese, M., 2022. Trehalose treatment in zebrafish model of Lafora disease. Int. J. Mol. Sci. 23 (12), 6874. https://doi.org/10.3390/ijms23126874.
Di Giorgi, N., Cecchettini, A., Michelucci, E., Signore, G., Ceccherini, E., Ferro, F., Elefante, E., Tani, C., Baldini, C., Rocchiccioli, S., 2022. Salivary proteomics markers for preclinical Sjögren's syndrome: a pilot study. Biomolecules 12 (6), 738. https://doi.org/10.3390/biom12060738.
Di Nottia, M., Marchese, M., Verrigni, D., Mutti, C.D., Torraco, A., Oliva, R., Fernandez-Vizarra, E., Morani, F., Trani, G., Rizza, T., Ghezzi, D., Ardissone, A., Nesti, C., Vasco, G., Zeviani, M., Minczuk, M., Bertini, E., Santorelli, F.M., Carrozzo, R., 2020. A homozygous MRPL24 mutation causes a complex movement disorder and affects the mitoribosome assembly. Neurobiol. Dis. 141, 104880 https://doi.org/10.1016/j.nbd.2020.104880.
di Ronza, A., Bajaj, L., Sharma, J., Sanagasetti, D., Lotfi, P., Adamski, C.J., Collette, J., Palmieri, M., Amawi, A., Popp, L., Chang, K.T., Meschini, M.C., Leung, H.E., Segatori, L., Simonati, A., Sifers, R.N., Santorelli, F.M., Sardiello, M., 2018. CLN8 is an endoplasmic reticulum cargo receptor that regulates lysosome biogenesis. Nat. Cell Biol. 20 (12), 1370–1377. https://doi.org/10.1038/s41556-018-0228-7.
Dirac-Svejstrup, A.B., Walker, J., Faull, P., Encheva, V., Akimov, V., Puglia, M., Perkins, D., Kümper, S., Hunjan, S.S., Blagoev, B., Snijders, A.P., Powell, D.J., Svejstrup, J.Q., 2020. DDI2 is a ubiquitin-directed Endoprotease responsible for cleavage of transcription factor NRF1. Mol. Cell 79 (2), 332–341.e7. https://doi.org/10.1016/j.molcel.2020.05.035.
Doccini, S., Marchese, M., Morani, F., Gammaldi, N., Mero, S., Pezzini, F., Soliymani, R., Santi, M., Signore, G., Ogi, A., Rocchiccioli, S., Kanninen, K.M., Simonati, A., Lalowski, M.M., Santorelli, F.M., 2022. Lysosomal proteomics links disturbances in lipid homeostasis and sphingolipid metabolism to CLN5 disease. Cells 11 (11), 1840. https://doi.org/10.3390/cells11111840.
Galizzi, G., Russo, D., Deidda, I., Cascio, C., Passantino, R., Guarneri, R., Bigini, P., Mennini, T., Drago, G., Guarneri, P., 2011. Different early ER-stress responses in the CLN8(mnd) mouse model of neuronal ceroid lipofuscinosis. Neurosci. Lett. 488 (3), 258–262. https://doi.org/10.1016/j.neulet.2010.11.041.
Grone, B.P., Marchese, M., Hamling, K.R., Kumar, M.G., Krasniak, C.S., Sicca, F., Santorelli, F.M., Patel, M., Baraban, S.C., 2016. Epilepsy, behavioral abnormalities, and physiological comorbidities in Syntaxin-binding protein 1 (STXBP1) mutant zebrafish. PLoS ONE 11 (3), e0151148. https://doi.org/10.1371/journal.pone.0151148.
Huang, Y., Cartlidge, R., Walpitagama, M., Kaslin, J., Campana, O., Wlodkowic, D., 2018. Unsuitable use of DMSO for assessing behavioral endpoints in aquatic model species. Sci. Total Environ. 615, 107–114. https://doi.org/10.1016/j.scitotenv.2017.09.260.
Huber, R.J., Hughes, S.M., Liu, W., Morgan, A., Tuxworth, R.I., Russell, C., 2020. The contribution of multicellular model organisms to neuronal ceroid lipofuscinosis research. Biochim. Biophys. Acta Mol. basis Dis. 1866 (9), 165614 https://doi.org/10.1016/j.bbadis.2019.165614.
Katz, M.L., Rustad, E., Robinson, G.O., Whiting, R.E.H., Student, J.T., Coates, J.R., Narfstrom, K., 2017. Canine neuronal ceroid lipofuscinoses: promising models for preclinical testing of therapeutic interventions. Neurobiol. Dis. 108, 277–287. https://doi.org/10.1016/j.nbd.2017.08.017.
Kim, W.D., Wilson-Smillie, M.L.D.M., Thanabalasingam, A., Lefrancois, S., Cotman, S.L., Huber, R.J., 2022. Autophagy in the neuronal ceroid Lipofuscinoses (batten disease). Front. Cell Dev. Biol. 10, 812728 https://doi.org/10.3389/fcell.2022.812728.
Kolikova, J., Afzalov, R., Surin, A., Lehesjoki, A.E., Khiroug, L., 2011. Deficient mitochondrial ca(2+) buffering in the Cln8(mnd) mouse model of neuronal ceroid lipofuscinosis. Cell Calcium 50 (6), 491–501. https://doi.org/10.1016/j.ceca.2011.08.004.
Leinonen, H., Keksa-Goldsteine, V., Ragauskas, S., Kohlmann, P., Singh, Y., Savchenko, E., Puranen, J., Malm, T., Kalesnykas, G., Koistinaho, J., Tanila, H., Kanninen, K.M., 2017. Retinal degeneration in a mouse model of CLN5 disease is associated with compromised autophagy. Sci. Rep. 7 (1), 1597. https://doi.org/10.1038/s41598-017-01716-1.
Li, J., Deffieu, M.S., Lee, P.L., Saha, P., Pfeffer, S.R., 2015. Glycosylation inhibition reduces cholesterol accumulation in NPC1 protein-deficient cells. Proc. Natl. Acad. Sci. USA 112 (48), 14876–14881. https://doi.org/10.1073/pnas.1520490112.
Livak, K.J., Schmittgen, T.D., 2001. Analysis of relative gene expression data using real-time quantitative PCR and the 2(-Delta Delta C(T)). Method Methods (San Diego, Calif.) 25 (4), 402–408. https://doi.org/10.1006/meth.2001.1262.
MacRae, C.A., Peterson, R.T., 2015. Zebrafish as tools for drug discovery. Nat. Rev. Drug Discov. 14 (10), 721–731. https://doi.org/10.1038/nrd4627.
Mahmood, F., Fu, S., Cooke, J., Wilson, S.W., Cooper, J.D., Russell, C., 2013. A zebrafish model of CLN2 disease is deficient in tripeptidyl peptidase 1 and displays progressive neurodegeneration accompanied by a reduction in proliferation. Brain J. Neurol. 136 (Pt 5), 1488–1507. https://doi.org/10.1093/brain/awt043.
Marchese, M., Pappalardo, A., Baldacci, J., Verri, T., Doccini, S., Cassandrini, D., Bruno, C., Fiorillo, C., Garcia-Gil, M., Bertini, E., Pitto, L., Santorelli, F.M., 2016. Dolichol-phosphate mannose synthase depletion in zebrafish leads to dystrophic muscle with hypoglycosylated α-dystroglycan. Biochem. Biophys. Res. Commun. 477 (1), 137–143. https://doi.org/10.1016/j.bbrc.2016.06.033.
Marotta, D., Tinelli, E., Mole, S.E., 2017. NCLs and ER: a stressful relationship. Biochimica et biophysica acta. Mol. Basis Dis. 1863 (6), 1273–1281. https://doi.org/10.1016/j.bbadis.2017.04.003.
Masek, M., Zang, J., Mateos, J.M., Garbelli, M., Ziegler, U., Neuhauss, S.C.F., Bachmann-Gagescu, R., 2023. Studying the morphology, composition and function of the photoreceptor primary cilium in zebrafish. Methods Cell Biol. 175, 97–128. https://doi.org/10.1016/bs.mcb.2022.10.004.
Messer, A., Flaherty, L., 1986. Autosomal dominance in a late-onset motor neuron disease in the mouse. J. Neurogenet. 3 (6), 345–355. https://doi.org/10.3109/01677068609106858.
Morsy, A., Carmona, A.V., Trippier, P.C., 2021. Patient-derived induced pluripotent stem cell models for phenotypic screening in the neuronal ceroid Lipofuscinoses. Molecules (Basel, Switzerland) 26 (20), 6235. https://doi.org/10.3390/molecules26206235.
Naef, V., Marchese, M., Ogi, A., Fichi, G., Galatolo, D., Licitra, R., Doccini, S., Verri, T., Argenton, F., Morani, F., Santorelli, F.M., 2021. Efficient neuroprotective rescue of sacsin-related disease phenotypes in zebrafish. Int. J. Mol. Sci. 22 (16), 8401. https://doi.org/10.3390/ijms22168401.
Nita, D.A., Mole, S.E., Minassian, B.A., 2016. Neuronal ceroid lipofuscinoses. Epilept. Disord. 18 (S2), 73–88. https://doi.org/10.1684/epd.2016.0844.
Passantino, R., Cascio, C., Deidda, I., Galizzi, G., Russo, D., Spedale, G., Guarneri, P., 2013. Identifying protein partners of CLN8, an ER-resident protein involved in neuronal ceroid lipofuscinosis. Biochim. Biophys. Acta 1833 (3), 529–540. https://doi.org/10.1016/j.bbamcr.2012.10.030.
Pesaola, F., Quassollo, G., Venier, A.C., De Paul, A.L., Noher, I., Bisbal, M., 2021. The neuronal ceroid lipofuscinosis-related protein CLN8 regulates endo-lysosomal dynamics and dendritic morphology. Biol. Cell. 113 (10), 419–437. https://doi.org/10.1111/boc.202000016.
Pupyshev, A.B., Klyushnik, T.P., Akopyan, A.A., Singh, S.K., Tikhonova, M.A., 2022. Disaccharide trehalose in experimental therapies for neurodegenerative disorders: molecular targets and translational potential. Pharmacol. Res. 183, 106373 https://doi.org/10.1016/j.phrs.2022.106373.
Ranta, S., Zhang, Y., Ross, B., Lonka, L., Takkunen, E., Messer, A., Sharp, J., Wheeler, R., Kusumi, K., Mole, S., Liu, W., Soares, M.B., Bonaldo, M.F., Hirvasniemi, A., de la Chapelle, A., Gilliam, T.C., Lehesjoki, A.E., 1999. The neuronal ceroid lipofuscinoses in human EPMR and mnd mutant mice are associated with mutations in CLN8. Nat. Genet. 23 (2), 233–236. https://doi.org/10.1038/13868.
Rogowski, M., Bellusci, L., Sabatini, M., Rapposelli, S., Rahman, S.M., Chiellini, G., Assadi-Porter, F.M., 2019. Lipolytic effects of 3-Iodothyronamine (T1AM) and a novel thyronamine-like analog SG-2 through the AMPK pathway. Int. J. Mol. Sci. 20 (16), 4054. https://doi.org/10.3390/ijms20164054.
Runfola, M., Perni, M., Yang, X., Marchese, M., Bacci, A., Mero, S., Santorelli, F.M., Polini, B., Chiellini, G., Giuliani, D., Vilella, A., Bodria, M., Daini, E., Vandini, E., Rudge, S., Gul, S., Wakelam, M.O.J., Vendruscolo, M., Rapposelli, S., 2021. Identification of a thyroid hormone derivative as a pleiotropic agent for the treatment of Alzheimer's disease. Pharmaceuticals (Basel, Switzerland) 14 (12), 1330. https://doi.org/10.3390/ph14121330.
Rupprecht, P., Prendergast, A., Wyart, C., Friedrich, R.W., 2016. Remote z-scanning with a macroscopic voice coil motor for fast 3D multiphoton laser scanning microscopy. Biomed. Opt. Exp. 7 (5), 1656–1671. https://doi.org/10.1364/BOE.7.001656.
Tóth, V., Vadászi, H., Ravasz, L., Mittli, D., Mátyás, D., Molnár, T., Micsonai, A., Szaniszló, T., Lőrincz, P., Kovács, R.Á., Juhász, T., Beke-Somfai, T., Juhász, G., Györffy, B.A., Kékesi, K.A., Kardos, J., 2022. Neuronal-specific septin-3 binds Atg8/

LC3B, accumulates and localizes to autophagosomes during induced autophagy. Cell. Mol. Life Sci. 79 (9), 471. https://doi.org/10.1007/s00018-022-04488-8.
Traina, G., Bigini, P., Federighi, G., Sitia, L., Paroni, G., Fiordaliso, F., Salio, M., Bendotti, C., Brunelli, M., 2012. Lipofuscin accumulation and gene expression in different tissues of mnd mice. Mol. Neurobiol. 45 (2), 247–257. https://doi.org/10.1007/s12035-012-8248-y.
Turner, C., Sawle, A., Fenske, M., Cossins, A., 2012. Implications of the solvent vehicles dimethylformamide and dimethylsulfoxide for establishing transcriptomic endpoints in the zebrafish embryo toxicity test. Environ. Toxicol. Chem. 31 (3), 593–604. https://doi.org/10.1002/etc.1718.
Wang, P., Long, M., Zhang, S., Cheng, Z., Zhao, X., He, F., Liu, H., Ming, L., 2017. Hypoxia inducible factor-1α regulates autophagy via the p27-E2F1 signaling pathway. Mol. Med. Rep. 16 (2), 2107–2112. https://doi.org/10.3892/mmr.2017.6794.
Wavre-Shapton, S.T., Calvi, A.A., Turmaine, M., Seabra, M.C., Cutler, D.F., Futter, C.E., Mitchison, H.M., 2015. Photoreceptor phagosome processing defects and disturbed autophagy in retinal pigment epithelium of Cln3Δex1-6 mice modelling juvenile neuronal ceroid lipofuscinosis (batten disease). Hum. Mol. Genet. 24 (24), 7060–7074. https://doi.org/10.1093/hmg/ddv406.
Westerfield, M., 2000. The Zebrafish Book. A Guide for the Laboratory Use of Zebrafish (*Danio rerio*), 4th edition. University of Oregon Press, Eugene.
Wu, J., Yang, Y., Sun, C., Sun, S., Li, Q., Yao, Y., Fei, F., Lu, L., Chang, Z., Zhang, W., Wang, X., Luo, F., 2017. Disruption of the gaa gene in zebrafish fails to generate the phenotype of classical Pompe disease. DNA Cell Biol. 36 (1), 10–17. https://doi.org/10.1089/dna.2016.3459.
Yuan, Q., Zeng, Z.L., Yang, S., Li, A., Zu, X., Liu, J., 2022. Mitochondrial stress in metabolic inflammation: modest benefits and full losses. Oxid. Med. Cell. Longev. 2022, 8803404 https://doi.org/10.1155/2022/8803404.
Zang, J., Neuhauss, S.C.F., 2021. Biochemistry and physiology of zebrafish photoreceptors. Pflugers Arch. Eur. J. Physiol. 473 (9), 1569–1585. https://doi.org/10.1007/s00424-021-02528-z.